photonics

MDPI

Article

A Tutorial on Retroreflectors and Arrays Used in Satellite and Lunar Laser Ranging

John J. Degnan †

Independent Researcher, Odenton, MD 21113, USA; jjdegnan3rd@gmail.com

† Semi-Retired Technical Consultant (2018-present) formerly held various research and supervisory positions at NASA Goddard Space Flight Center (1964–2002), Chief Scientist at Sigma Space Corporation, (2002–2018), and Distinguished Adjunct Professor of Physics at The American University (1988–1993). Cofounder of International Laser Ranging Service (1998) and 1st ILRS Governing Board Chairman (1998–2002), Optica Fellow. IEEE Senior Life Member.

Abstract: The present paper discusses the basics of retroreflector theory and the manner in which they are combined in arrays to service the laser tracking of artificial satellites and the Moon. We begin with a discussion of the relative advantages and disadvantages of solid versus hollow cube corners and the functional dependence of their optical cross-sections and far-field patterns on cube diameter. Because of velocity aberration effects, the design of an array for a particular space mission depends on many factors, including the desired range accuracy and the satellite's orbital altitude, velocity, and pass geometry relative to the tracking station. This generally requires the individual retroreflectors in the array to be "spoiled" by perturbing one or more of the 90-degree angles that define a perfect cube corner, or alternatively, by adding a curved surface to a hollow cube. In order to obtain adequate return signal strengths from all points along the satellite path, the rotational orientation of the retroreflectors within the array may need to be varied or "clocked". Possible approaches to developing millimeter-accuracy arrays with both large cross-sections and ultrashort satellite signatures are discussed, as are new designs proposed to replace aging reflectors on the Moon. Finally, we briefly discuss methods for laser ranging beyond the Moon.

Keywords: retroreflectors; cube corners; Satellite Laser Ranging; Lunar Laser Ranging; velocity aberration; spoiling; clocking; cross-section

Citation: Degnan, J.J. A Tutorial on Retroreflectors and Arrays Used in Satellite and Lunar Laser Ranging. *Photonics* **2023**, *10*, 1215. https://doi.org/10.3390/photonics10111215

Received: 13 September 2023
Revised: 23 October 2023
Accepted: 26 October 2023
Published: 31 October 2023

1. Introduction

The first successful Satellite Laser Ranging (SLR) experiment was carried out on 31 October 1964 by Dr. Henry H. Plotkin and his team at the NASA Goddard Space Flight Center in Greenbelt, Maryland, USA [1]. In this first experiment, the NASA Explorer 22B satellite was equipped with an array of retroreflectors designed to reflect laser pulses from a ground station back to their point of origin. The roundtrip distance to the satellite can then be determined by multiplying the roundtrip transit time by the speed of light. In 1969, a team led by Prof. Carroll Alley of the University of Maryland succeeded in ranging to a flat panel of 100 retroreflectors left on the lunar surface by NASA's Apollo 11 crew [2]. In the almost six decades since these early experiments, dozens of Earth-orbiting satellites carrying retroreflector arrays have been launched to support a wide variety of scientific investigations, and five arrays have been placed on the lunar surface by three manned US Apollo missions (11, 14, and 15) and two unmanned Soviet Lunakhod (17 and 21) missions carrying arrays provided by France. The present author has previously published a comprehensive review of the active ground-based SLR hardware and operations [3], whereas this paper will concentrate on the requirements placed on the passive spaceborne segment, i.e., the retroreflector arrays. For a more complete discussion of recent SLR capabilities and trends, the reader is referred to the following reviews [4,5].

2. SLR Link Equation

During the first four decades of SLR (1964 to 2004), ground stations were characterized by a moderate-to-large (submeter-to-meter-class) receiver telescope, and the laser beam was transmitted via a parallel, small-diameter tube mounted on the side of the telescope. Since the laser beam divergence is proportional to the ratio of the laser wavelength to the beam radius (λ/ω), this approach resulted in an unnecessarily high divergence beam that required much higher-energy lasers to obtain an adequate satellite return. These high-energy beams posed a potential eye safety hazard to personnel in low-flying aircraft and to ground personnel during ground calibrations. As a result, all early SLR stations were equipped with dedicated aircraft radars and safety personnel to man them. However, in 1994, the present author proposed a new system, SLR2000, to NASA management [6], which optimally sized and transmitted a low-divergence laser beam via a common transmit–receive telescope to achieve maximum illumination of the satellite array while simultaneously reducing the laser energy and the threat to eye safety. The optimum SLR2000 design drew heavily from earlier studies on optical antenna gain carried out in support of early NASA laser communications studies [7,8]. The NASA SLR2000 funding started slowly in 1998, but by 2003, the newly named Next-Generation Satellite Laser Ranging (NGSLR) system had tracked its first satellite and continued tracking until 2007, when it was sadly destroyed by a lightning bolt. NASA's replacement system, Space Geodesy Satellite Laser Ranging (SGSLR), adds additional automation and is currently being installed at three sites—(1) the NASA Goddard Space Flight Center in Greenbelt, MD, USA, (2) the McDonald Observatory at the University of Texas, USA, and (3) Ny Alesund, Norway [9].

The SLR link equation defines the number of photons detected by the ground station and is given by

$$n_s = \frac{E}{h\tau}\eta_t \frac{2}{\pi(\theta_d R)^2} exp\left[-2\left(\frac{\Delta\theta_p}{\theta_d}\right)^2\right]\left[\frac{1}{1+\left(\frac{\Delta\theta_j}{\theta_d}\right)^2}\right]\left(\frac{\sigma A_r}{4\pi R^2}\right)\eta_r\eta_d T_a^2 T_c^2 \quad (1)$$

where

n_s = the number of detected satellite photoelectrons per laser pulse
E_t = the laser pulse energy
$h\nu$ = the laser photon energy = 3.73×10^{-19} J @ 532 nm (Doubled Nd:YAG)
η_t = the transmitter optical throughput efficiency
θ_d = the Gaussian beam divergence half angle
R = the slant range between the station and satellite
$\Delta\theta_p$ = the laser beam pointing error
$\Delta\theta_j$ = the RMS tracking mount jitter
σ = the satellite optical cross-section
A_r = the telescope receiving area.
η_r= the receiver optical throughput efficiency
η_c = the detector counting efficiency
T_a = the one-way atmospheric transmission
T_c = the one-way cirrus cloud transmission

We note from Equation (1) that the received signal strength varies as $1/R^4$ and that the satellite optical cross-section, σ, is the sole contribution of the space segment to the link equation. Retroreflectors, also referred to as "cube corners", can be either hollow or solid, and the solid retros can be coated or uncoated. Table 1 provides a summary of the various retro types, their unique characteristics, and their historical usage. Note also that the satellite optical array cross-section, σ, is the sole link contribution of the space segment.

Table 1. Three types of cube corners and their properties.

Type	Al Back-Coated Solid	Uncoated Solid (TIR)	Hollow
Frequency of Use	Most Common	Occasional Use	Not currently used in the visible range
Satellite Examples	Most satellites	Apollo, LAGEOS, AJISAI, ETS-VIII	ADEOS RIS, REM, TES
Reflectivity, ρ	0.78	0.93	Can approach 1.0
Polarization Sensitive	No	Yes	No—metal coating Yes—dielectric coating
Weight	Heavy	Heavy	Light
Far-Field Pattern	Wide	Wide	Narrow
Issues	Metal coatings absorb sunlight and create thermal gradients. Not as well shielded at high orbital altitudes.	Fewer thermal problems, but TIR "leaks" at incidence angles > 17°. Polarization effects reduce cross-section by a factor of 4.	Thermal heating and gradient effects on joints

Retroreflectors (or "cube corners") are designed to reflect light back to the point of origin in a narrow beam. Increasing the size or number of retroreflectors increases the return signal strength. Figure 1 illustrates the two basic types of cube corner, i.e., solid or hollow. Table 1 lists the relevant properties and/or advantages of (1) aluminum back-coated solid retroreflectors, (2) uncoated solid Total Internal Reflection (TIR) retroreflectors, and (3) hollow retroreflectors. For normally incident light, a single unspoiled retroreflector (cube corner) has a peak, on-axis, optical cross-section defined by

$$\sigma_{cc} = \rho A_{cc}\left(\frac{4\pi}{\Omega}\right) = \rho\frac{4\pi A_{cc}^2}{\lambda^2} = \frac{\pi^3 \rho D^4}{4\lambda^2} \quad (2)$$

where the reflectivity of the cube corner, ρ, is typically equal to 0.78 or 0.93 for aluminum-coated back faces and uncoated Total Internal Reflection (TIR) surfaces, respectively, A_{cc} is the collecting aperture of the corner cube, D is the cube diameter, $4\pi/\Omega$ is the on-axis reflector gain, and Ω is the effective solid angle occupied by the far-field diffraction pattern (FFDP) of the retroreflector.

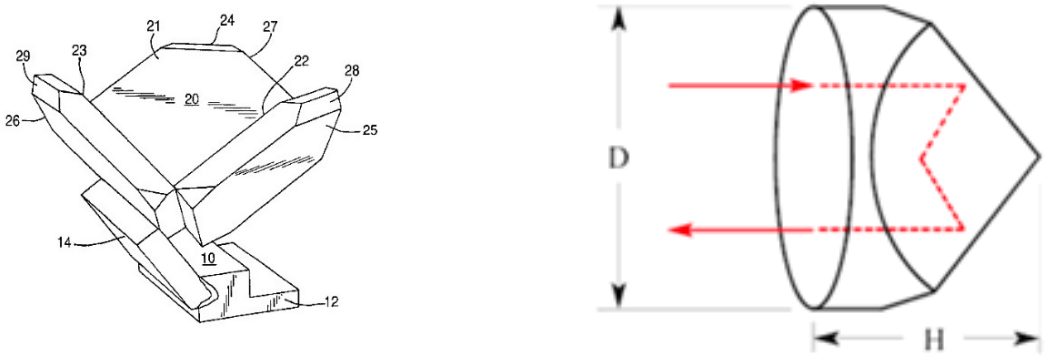

Figure 1. *Cont.*

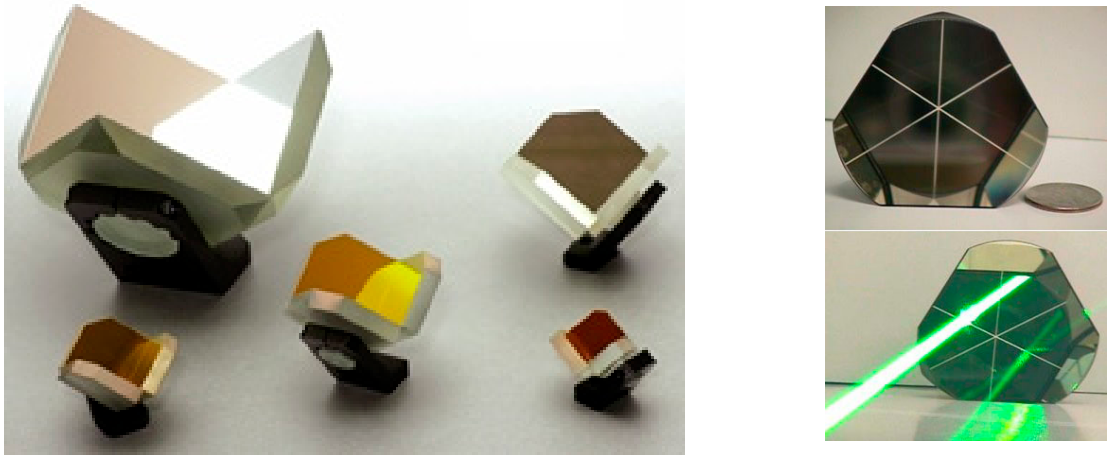

Figure 1. Two types of retroreflector/cube corner—hollow and solid.

As illustrated in Figure 2, the peak optical cross-section rises rapidly as the retroreflector diameter to the fourth power. For the popular 1.5 in (38 mm)-diameter cube with a physical cross-section of 0.001 m^2, the peak optical cross-section is about 5.8×10^7 m^2, an increase of over ten orders of magnitude.

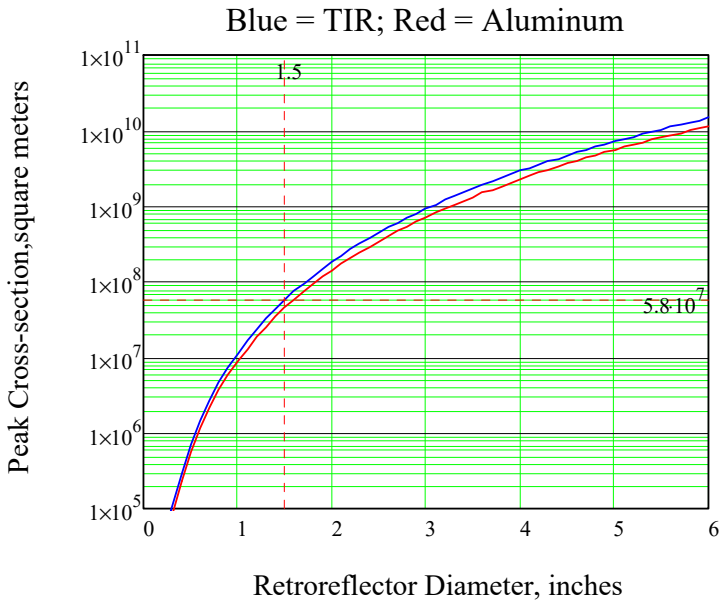

Figure 2. The peak cross-section in square meters as a function of the solid retroreflector diameter in inches for both Total Internal Reflection (blue curve) and aluminum back-coating (red curve) surfaces. The peak optical cross-section rises rapidly as the retroreflector diameter to the fourth power. For the popular 1.5 in (38 mm)-diameter cube with a physical cross-section of 0.001 m^2, the peak optical cross-section is about 5.8×10^7 m^2, an increase of over ten orders of magnitude.

3. Retroreflector Far-Field Diffraction Pattern (FFDP)

For a uniformly illuminated circular aperture, the FFDP of the reflected wave, as plotted in Figure 3, is the familiar Airy function, given by

$$\sigma(x) = \sigma_{cc}\left[\frac{2J_1(x)}{x}\right]^2 \quad (3)$$

$$x = \frac{\pi D}{\lambda} sin\theta \tag{4}$$

where the frequency-doubled Nd:YAG laser wavelength, λ = 532 nm, is the most widely used in the SLR ground network, and D is the cube aperture diameter.

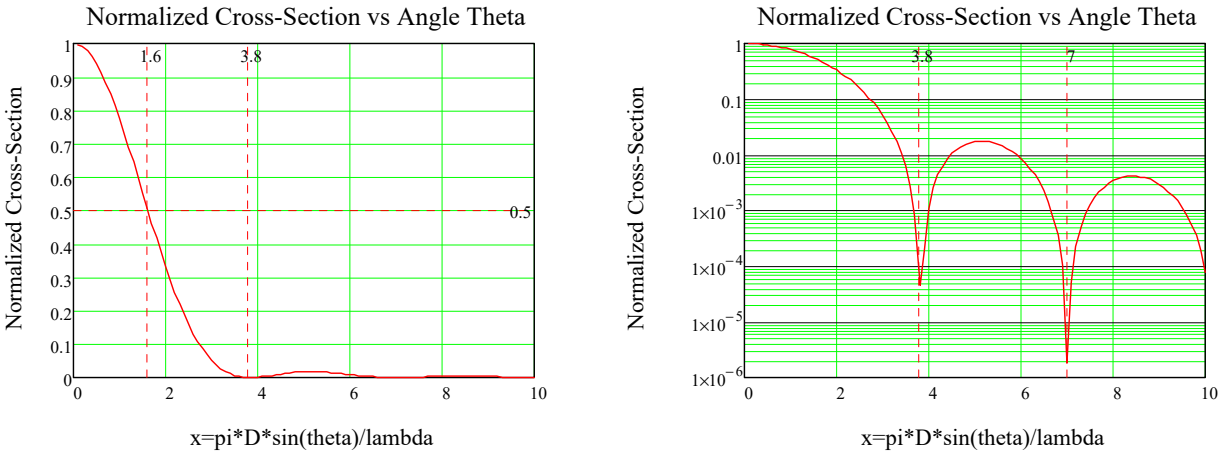

Figure 3. The FFDP of an unspoiled circular aperture retroreflector is plotted on a linear scale and a logarithmic scale in parts (**a**,**b**) of the figure, respectively. The half-power and first null occur at x = 1.6 and 3.8, respectively. For the popular 1.5 in (38 mm)-diameter cube at 532 nm, this corresponds to θ = 7.1 and 16.9 microradians (1.5 and 3.5 arcsec), respectively.

At an arbitrary incidence angle, θ_{inc}, the effective area of the cube is reduced by the factor

$$\eta(\theta_{inc}) = \frac{2}{\pi}\left(sin^{-1}\mu - \sqrt{2}tan\theta_{ref}\right)cos\theta_{inc} \tag{5}$$

where θ_{inc} is the incidence angle and θ_{ref} is the internal refracted angle, as determined by Snell's Law, i.e.,

$$\theta_{ref} = sin^{-1}\left(\frac{sin\theta_{inc}}{n}\right) \tag{6}$$

where n is the cube index of refraction, and the quantity μ is given by the formula

$$\mu = \sqrt{1 - tan^2\theta_{ref}} \tag{7}$$

Thus, as the incidence angle, θ_{inc}, increases, the peak optical cross-section in the center of the reflected lobe falls off as

$$\sigma_{eff}(\theta_{inc}) = \eta^2(\theta_{inc})\sigma_{cc} \tag{8}$$

and is plotted in Figure 4.

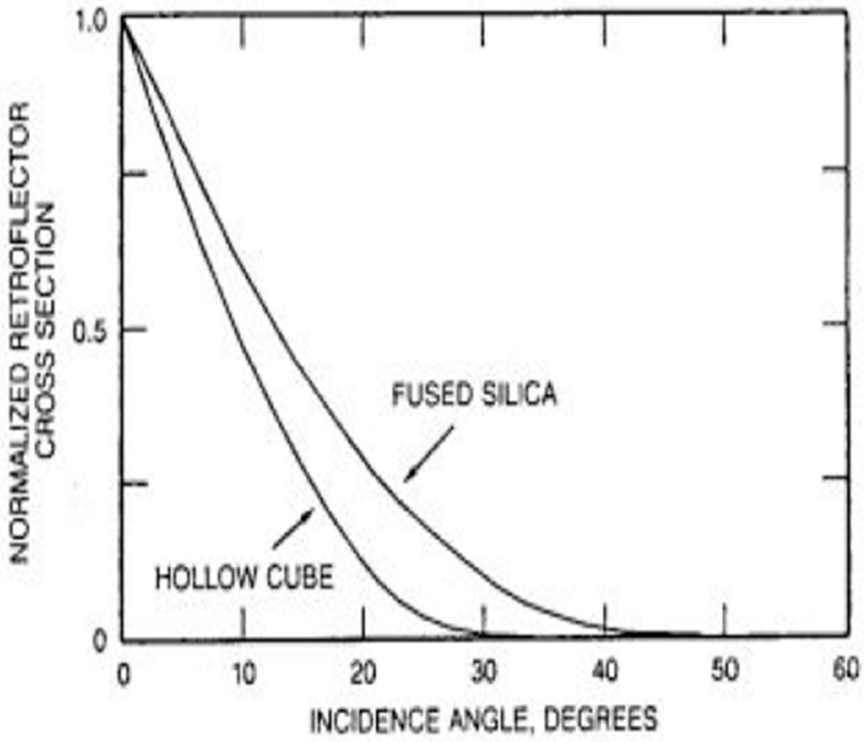

Figure 4. The normalized cross-section as a function of beam incidence angle for hollow and solid fused silica retroreflectors. The 50% and 0% efficiency points for fused silica (n = 1.455) are 13° and 45°, respectively, whereas the 50% and 0% efficiency points for a hollow cube (n = 1) are 9° and 31°, respectively, i.e., hollow cubes have a narrower angular response range than solid cubes.

4. Retroreflectors as Ground Calibration Targets

All SLR stations make use of a calibration scheme to initially determine and then monitor changes in optical and/or electronic system delays that might be caused by changes in hardware or environmental conditions (e.g., temperature). The most common approach is to place a single retroreflector at some carefully surveyed distance from the ground station "invariant point", defined as the intersection of the elevation and azimuth axes of the telescope assembly. The retro acts as a point source with a delta function response. This calibration distance is usually measured at the 1 or 2 mm level using accurate ground surveying techniques. Subtracting the known target range from the measured range provides a "range correction" which is then applied to all future satellite measurements. For maximum accuracy, calibrations are typically performed hourly.

5. Science Applications of SLR Impact the Satellite Array Design

The current SLR constellation spans a wide range of altitudes (500 km to 36,000 km) and inclinations depending on mission requirements, and each retroreflector array has to be designed accordingly based on orbital altitude, mission goals, desired signal strength, etc. The artificial satellites typically fall into four altitude realms with very different scientific goals, e.g.,

1. **Low-Earth Orbiting (LEO: h < 1500 km):** Earth gravity field studies and/or orbital support for spaceborne radars or lidars observing terrain heights, sea/ice levels, tree mass, etc.
2. **Medium Earth Orbiting (MEO: h~6000 km):** Low-drag MEO satellites such as LAGEOS 1 and 2 are ideal for accurately determining relative station positions, tectonic plate motion, regional crustal deformation, etc.
3. **Global Navigation System Satellites (GNSS: h~20,000 km):** SLR provides precise orbital support to International Navigation Constellations, such as GLONASS (Rus-

sia), GALILEO (EU), and COMPASS/BeiDou (China). All of the satellites in the aforementioned constellations are, or will be, equipped with laser retroreflectors, thereby enhancing the accuracy of GNSS orbits and their associated ground networks and transportation guidance. Only two of the US GPS satellites carry retroreflectors.

4. **Geosynchronous satellites (GEO: h~36,000 km):** in equatorial orbits provide continuous monitoring of roughly a third of the Earth's surface. Besides obvious defense and military applications, civilian applications include global communications, weather forecasting, television broadcasting, as well as communications between ground stations and/or relaying information between other satellites or spacecraft.

For maximum accuracy in orbit determination, the distance of the effective light reflection point from the satellite center of mass is ideally independent of the viewing angle. Thus, passive LEO and GEO satellites are typically spheres embedded with retros. Furthermore, since the signal strength decreases with satellite range as $1/R^4$, the sphere diameter typically increases with altitude to accommodate more retros in order to meet cross-section (signal strength) requirements. To improve detection probability and range precision, modern SLR stations typically employ fast, single-photon-sensitive, ultralow-timewalk detectors such as Micro Channel Plate Photo Multiplier Tubes (MCP/PMTs) or Single Photon Avalanche Diode (SPAD) arrays. When operated at or near single-photon-return levels, these detectors have allowed satellite detection at few kHz rates with low laser pulse energies as opposed to the historical few pulses per second with high pulse energies [6]. In the kHz low-signal scenario, each retroreflector in the array has a diminishing probability of providing the detected photon in a given measurement as it is further displaced from the laser line-of-sight (retro #7) and the laser beam incidence angle increases (Figure 5).

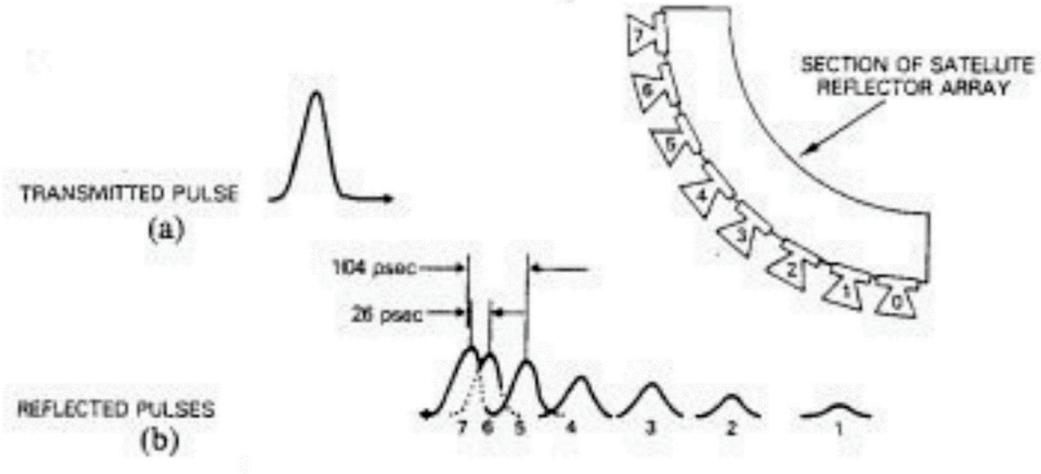

Figure 5. Pulse spreading induced by spherical LEO and GEO satellites (**a**). In multiphoton detection mode, the returned light pulse is the sum of the ultrashort (~100 psec) light pulses generated by the individual retroreflectors, which are reduced in intensity at the higher beam incidence angles (**b**). In multiphoton mode, the detector in the ground station sums over the individual retro returns before sending them to the timing electronics, thereby degrading the range precision. In single-photon mode, returns from individual reflectors are received at kHz rates and averaged over time to form "Normal Points".

In Figure 6, τ is a time normalized to the time it takes a light pulse to travel the diameter of the satellite, i.e., $2R_s/c$, where R_s is the radius of the sphere. Increasing the radius of the satellite will increase the cross-section by allowing the impinging laser beam to illuminate more cubes at low incidence angles. At the same time, however, the larger satellite will also broaden the impulse response, thereby degrading range precision. However, one can narrow the temporal response of the larger-diameter satellite while maintaining a high cross-section at low incidence angles by either using hollow rather than solid cube corners (as illustrated in Figure 6) or by recessing solid cubes inside hollow tubes to limit

the response to cubes within a narrower range of incidence angles. The latter approaches effectively eliminate the weaker contributions of the pulses to the right in Figure 5b.

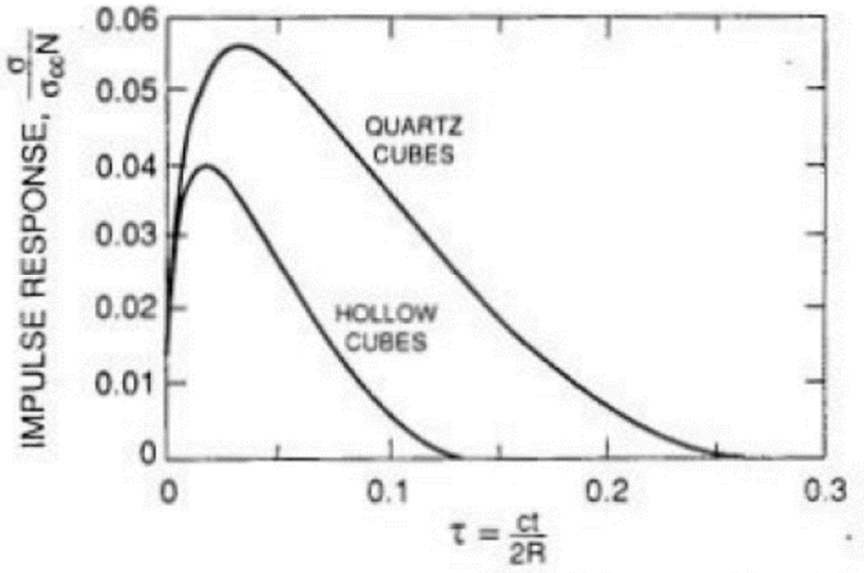

Figure 6. Impulse response in the large spherical satellite limit ($R_s >> nL$) for both hollow and solid quartz cube corners. The difference is due to the smaller acceptance angle in hollow cubes resulting in fewer cubes contributing to the return.

Finally, because GNSSs and geosynchronous satellites generally perform a utilitarian function (e.g., Earth observation, communications, navigation, etc.), the nadir side of the satellite approximately faces the Earth Center of Mass (CoM). For the typical maximum zenith tracking angle of 70°, the beam incidence angles from the array normal can vary from 0 to β, where

$$\beta = asin\left[\frac{R_E}{R_E + h} sin110^\circ\right] \quad (9)$$

For GNSS satellites at h = 20,000 km, β = 13.1 deg, and for GEO satellites at $h = 36,000$km, β = 8.2 deg. The smaller range of incidence angles ensures: (1) near-maximum-strength returns from a planar array; and (2) limited pulse spreading, especially if the array is compact in size and the retros are densely packed together to achieve the required cross-section. Nevertheless, the maximum flat-panel-induced laser pulse spreading per linear foot of array due to the zenith tracking angle is still 474 psec (7 cm) and 292 psec (4.4 cm) for GNSS and GEO satellites, respectively. Thus, typical rectangular or square planar arrays can introduce an angle-dependent broadening of the pulse return, resulting in lower-ranging precision. Although a planar circular array with the same area would result in more uniform pulse spreading, the use of a segmented sphere mounted on the nadir face of the satellite would largely eliminate angle-dependent pulse spreading and range biases.

6. Velocity Aberration and "Spoiled" Retroreflectors

If there is no relative velocity between the station and satellite, the beam reflected by the retroreflector will fall directly back onto the station. However, as illustrated in Figure 7, a relative velocity, v, between the satellite and station causes the reflected beam to be angularly deflected from the station in the forward direction of the satellite motion by an angle $\alpha = 2v/c$. This phenomenon is referred to as "velocity aberration". Since small-diameter cubes have small optical cross-sections but large-angle far-field diffraction patterns (FFDPs), the signal at the station is not significantly reduced by velocity aberration. On the other hand, large-diameter cubes with high cross-sections have small-angle FFDPs, and the signal at the station is therefore substantially reduced by velocity aberra-

tion. In general, the signal is reduced by half or more if the cube diameter, D_{cc}, satisfies the inequality

$$D_{cc} > D_{1/2} = \frac{1.6\,\lambda}{\pi\alpha} = \frac{0.8\,\lambda c}{\pi v} \tag{10}$$

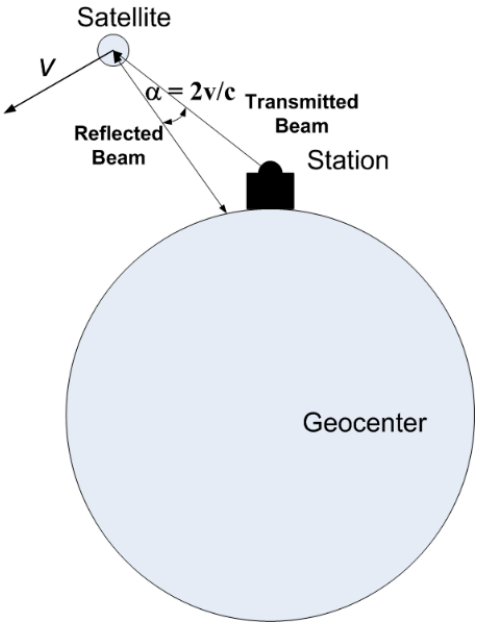

Figure 7. Velocity aberration causes the reflected beam to be angularly displaced from the ground station in the direction of the satellite velocity.

If there is a relative velocity between the satellite and the station, the coordinates of the FFDP are translated in the direction of the velocity vector. The magnitude of the angular displacement in the FFDP is given by

$$\alpha(h_s, \theta_{zen}, \omega) = \alpha_{max}(h_s)\sqrt{cos^2\omega + \Gamma^2(h_s, \theta_{zen})sin^2\omega} \tag{11}$$

where the maximum and minimum angular displacement values are given by

$$\begin{aligned} \alpha_{max}(h_s) &= \alpha(h_s, 0, 0) = \tfrac{2v_s}{c} = \tfrac{2}{c}\sqrt{\tfrac{gR_E^2}{R_E+h_s}} \\ \alpha_{min}(h_s) &= \alpha(h_s, 70^\circ, 90^\circ) = \alpha_{\max}(h_s)\,\Gamma(h_s, 70^\circ) \\ \Gamma(h_s, \theta_{zen}) &= \sqrt{1 - \left(\tfrac{R_E\, sin\theta_{zen}}{R_E+h_s}\right)^2} \\ \omega &= cos^{-1}\left[\left(\hat{r}\; x\; \hat{p}\right) * \hat{v}\right] \end{aligned} \tag{12}$$

where v = the satellite velocity at an altitude h_s above sea level, R_E = the Earth's radius = 6378 km, g = the surface gravity acceleration = 9.8 m/s^2, c = the velocity of light = 3×10^8 m/s, θ_{zen} = the largest satellite zenith angle for tracking = 70°, $\hat{r}$ = the unit vector to the satellite from the geocenter, $\hat{p}$ = the unit vector from the station to the satellite, and $\hat{v}$ = unit vector in the direction of the satellite velocity. The maximum and minimum values of the parameter α are plotted in Figure 8 as a function of the satellite altitude above sea level, h_s.

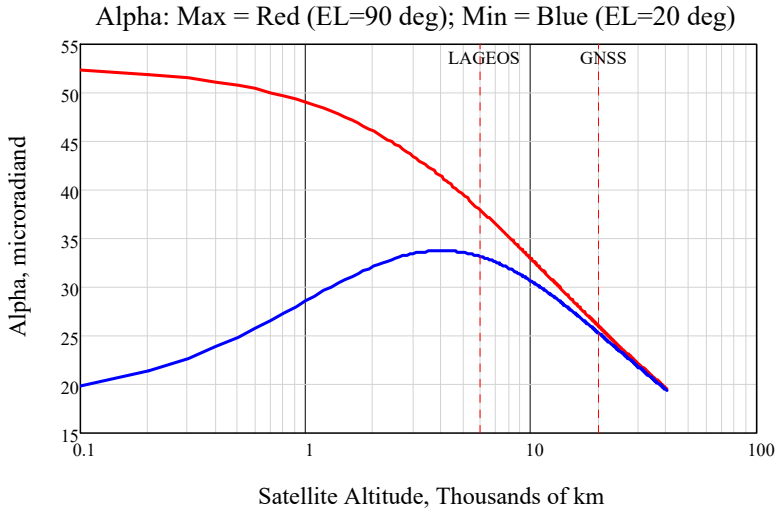

Figure 8. The maximum (red) and minimum (blue) values of the parameter α as a function of the satellite altitude, h_s. By the time one reaches geosynchronous altitude of 36,000 km, the two curves converge to roughly the same value of α.

"Spoiling" of the retroreflector is used to compensate for velocity aberration and improve the signal return from the satellite over the full range of observation angles. If we offset one or more (N = 1 to 3) of the cube dihedral angles from 90° by an amount δ, the central lobe of the FFDP splits into 2N spots, as in Figure 9. If n is the cube index of refraction, the mean angular distance of the lobe from the center of the original Airy pattern increases linearly with the dihedral angle offset, δ, according to

$$\gamma = \frac{4}{3}\sqrt{6}n\delta = 3.27\ n\ \delta \tag{13}$$

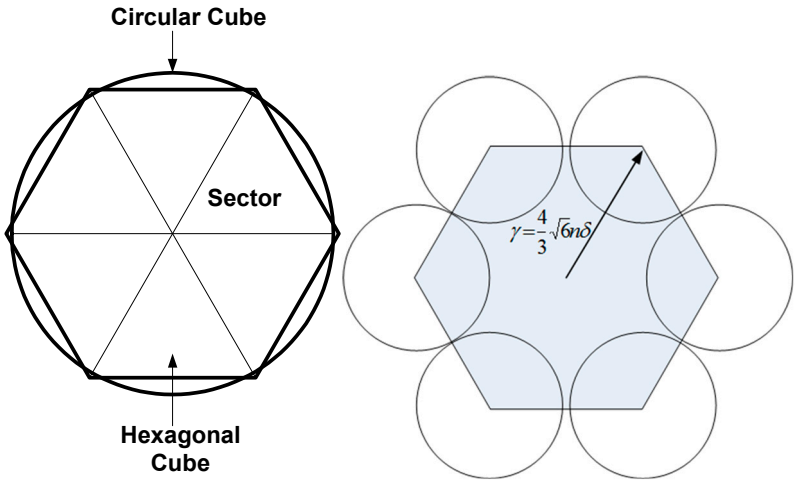

Figure 9. Far-field diffraction pattern (FFDP) of a retroreflector "spoiled" in all three axes. To simplify the drawing, the six resulting lobes are shown as circles, but, in reality, they are better described by the two-dimensional Fourier transform of either a triangular aperture or a 60-degree sector of a circle.

As before, the angular size of any given lobe decreases as the cube diameter gets larger, and the FFDP of each lobe is the 2D Fourier transform of an individual 60° sector. The energy distribution is complex but has a hexagonal symmetry if all three δs are equal. Furthermore, the effective area and peak cross-section of each lobe is reduced to

$$A_{eff} = \eta(\theta_{inc}) \frac{A_{cc}}{2N} \tag{14a}$$

and

$$\sigma_{peak} = \eta^2(\theta_{inc}) \frac{\sigma_{cc}}{(2N)^2} \tag{14b}$$

Since the return signal is weakest at the lowest elevation tracking angle, choosing $\gamma = \alpha_{min}$ places the peak of the lobe there, but any lobe energy inside the dark inner ring or outside the dark outer ring is wasted. Filling in the circumferential gaps between the lobes produced by 'spoiling" can be accomplished by rotating cubes by an angle equal to 60° divided by an integer greater than one, generally referred to as "clocking". A larger-diameter cube will result in smaller lobe dimensions and will reduce the spillover into the region outside the active angular ring, but it may also create a larger angular spacing between lobes, which in turn may require more clocking positions, as shown in Figure 10.

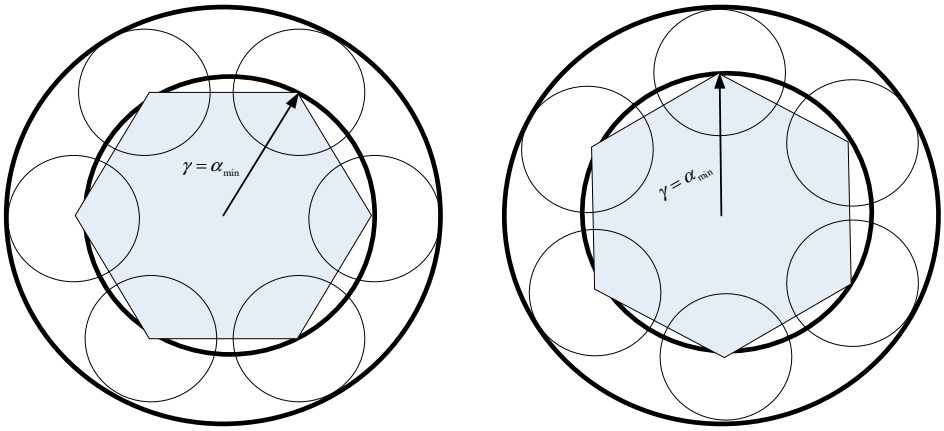

Figure 10. Example of "clocking" where two adjacent "spoiled" retroreflectors are rotated by 30 degrees with respect to one another in order to fill in potential gaps in the array FFDP due to "spoiling". The angular radius to the inner and outer dark circles in the figure correspond to the minimum and maximum values of α plotted in Figure 8.

7. Lunar Laser Ranging

Lunar Laser Ranging (LLR: h~384,000 km) tracks the distance and angular position of the surface retroreflector array relative to the Earth-based ground station and contributes to a wide range of applications, including astronomy, lunar science, gravitational physics, geodesy, and geodynamics [10]. From Equation (1), the return signal strength varies as $1/R^4$, and typically meter-class telescopes, combined with relatively high-energy lasers, were required to achieve detectable signals.

The earliest lunar-range measurements were conducted in 1962 by MIT Lincoln Laboratories by reflecting high-energy laser pulses (50 Joules) off the lunar surface and recording the received photons [11]. Subsequently, in 1969, in order to reduce the ground station telescope and laser energy requirements and simultaneously improve range accuracy to a specific lunar location, an array of one hundred 38 mm-diameter retroreflectors was placed on the lunar surface by the manned NASA Apollo 11 mission. In subsequent years, two other manned Apollo missions (14 and 15) also placed retroreflector panels on the Moon. Of these, the Apollo 15 array was the largest (300 vs. 100 cubes), thereby increasing the effective array cross-section (and return signal strength) by a factor of three relative to the earlier Apollo 11 and 14 arrays. Two unmanned Soviet Lunakhod (17 and 21) missions also landed arrays provided by France. Images of the current arrays and their locations on the lunar surface are provided in Figure 11.

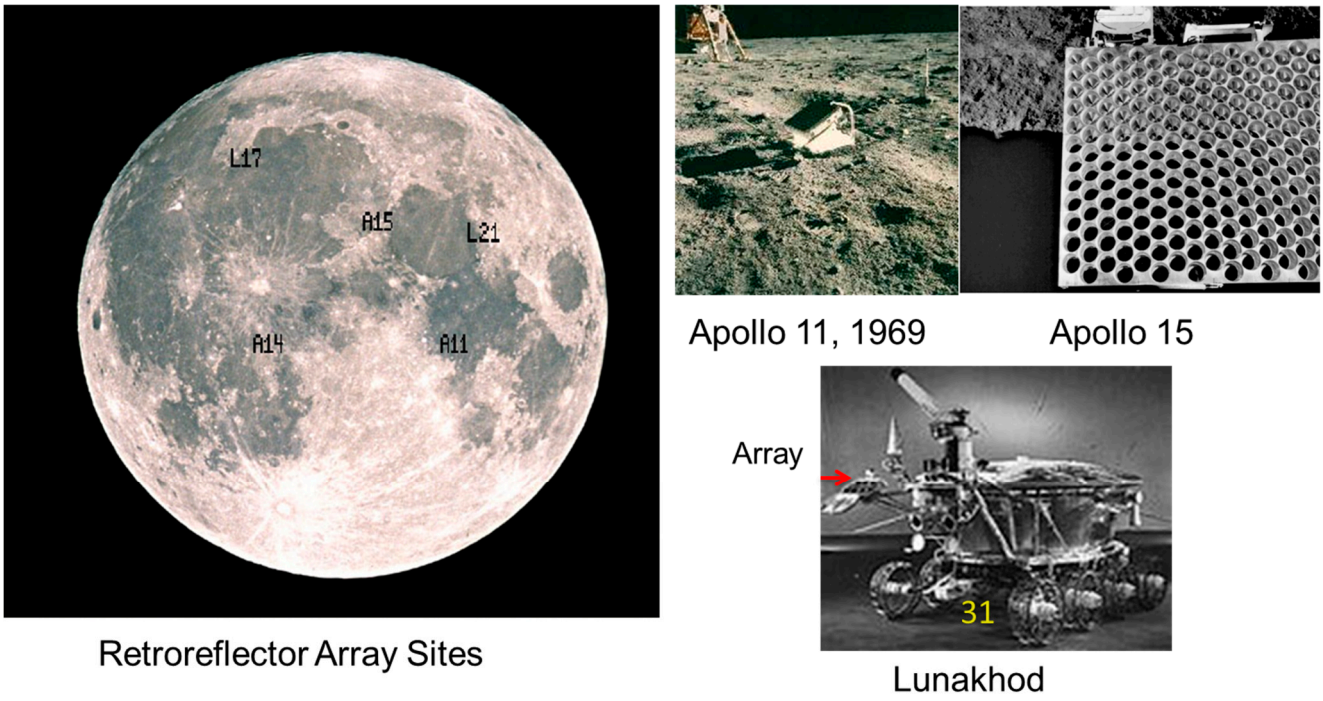

Figure 11. Images and locations of current lunar retroreflector arrays.

Although the Moon presents the same face to the Earth at all times, the angular velocity of the arrays as viewed by a particular Earth station varies slightly on a monthly basis due to a varying lunar velocity resulting from the Moon's slightly elliptical orbit about the Earth and, on a daily basis, due to the Earth's rotation about its polar axis. The Earth station velocity decreases with station latitude and also with time as the Moon approaches the station horizon. Fortunately, the beams reflected from the small-diameter (D_{cc} = 38 mm) cubes used in the current lunar arrays are highly divergent (on the order of $4\lambda/D_{cc}$ = 4 (532 nm/38 mm) = 56 μrad for the widely used 532 nm wavelength), and therefore velocity aberration has minimal effect on the cube performance. On the negative side, the high divergence of the retros also meant that many reflectors would be required to achieve measurable return signals, and, as discussed previously in Section 5 of this paper, the larger panels produce more pulse spreading at increasingly large incidence angles, resulting in diminished range precision.

Using the Earth–moon distance, $R_{EM} = h + R_E = 384.4 \times 10^6$ m, in Equation (12), we obtain α_{max} = 6.74 μrad or 1.40 arcsec and α_{min} = 6.68 μrad or 1.39 arcsec at an elevation angle of 20 degrees, where the relative velocity between the lunar target and the Earth ground station due to lunar orbital motion v = 1 km/s.

However, the latter equations ignore the smaller contribution of the station's motion due to the Earth's rotation (~0.46 km/s) to the relative velocity, which typically reduces α to 4 or 5 μrad for LLR but is negligible for LEO to GEO satellites. If the Apollo reflector arrays are pointed at the center of the Earth, the maximum beam incidence angle on the array from any Earth station (ignoring lunar libration) is

$$\theta_{inc} = atan\left(\frac{R_E}{R_{EM}}\right) = 0.95\ deg \tag{15}$$

and the unspoiled cube diameter for which the cross-section falls to half its peak value is $D_{1/2}$ = 40.6 mm = 1.6 inches, but the typical manufacturing tolerances are 0.5 arc-sec for dihedral angles and $\lambda/10$ for surface flatness. Apollo 15 has a flat array of three hundred 38 mm fused quartz cubes, each with an unspoiled peak cross-section of 5.8×10^7 m^2. Thus, the theoretical array cross-section, ignoring manufacturing tolerances

and local environmental effects, is $\sigma \cong 300(0.5)(5.8 \times 10^7\ m^2) = 8.7 \times 10^9\ m^2$. According to Arnold [12], polarization losses due to the uncoated TIR faces reduce the cross-section by a factor of four, resulting in $\sigma = 2.2 \times 10^9\ m^2$, but the International Laser Ranging Service (ILRS) lists a slightly lower Apollo 15 array cross-section of $\sigma = 1.4 \times 10^9\ m^2$.

For the first 30 years following the Apollo 11 landing, the vast majority of the LLR data set was provided by three stations equipped with meter class telescopes, i.e., (1) the 2.7 m MLRS telescope at the University of Texas McDonald Observatory, (2) the 1.5 m CERGA LLR telescope in Grasse, France, and (3) the 1.8 m University of Hawaii telescope on Mt. Haleakala. The latter site was decommissioned by NASA in 1992, but, since that time, two additional LLR sites have been added: (4) MLRO, Matera, Italy, and (5) the 3.5 m Apollo telescope located at Apache Point, New Mexico, USA. The large 3.5 m telescope at the Apache Point site resulted in multiphoton returns and unprecedented lunar-range precisions at the 1 to 3 mm level [13].

Since the turn of the century, more efficient, single, large retroreflectors have been proposed by various international teams to replace the large Apollo 15 array on future lunar-landing missions [14–19]. Whereas each of the 300 38 mm-diameter retroreflectors in the Apollo 15 array currently contributes about 0.33% to the overall signal seen by the ground stations due to the wide divergence angles of their reflected beams, no dihedral angle is required for small-diameter reflectors (<150 mm for coated and <100 mm for uncoated and hollow reflectors). However, since larger-diameter retroreflectors produce low-divergence reflected beams, they required dihedral angles of 0.20, 0.25, and 0.35 arcsec for coated, uncoated, and hollow reflectors, respectively. More recent publications provide updated analyses of these larger lunar reflectors [16,17].

8. Concluding Remarks

A common transmit–receive telescope maximizes the observed signal strength, allowing for the use of lower-power lasers and significantly higher measurement rates. Early SLR systems typically transmitted the quasi-Gaussian laser beam through a separate narrow parallel tube mounted on the receiving telescope. This resulted in a highly divergent transmitter beam with a full angular width equal to $4\lambda/D_b$ in our link equation, Equation (1), where D_b is the exiting laser beam diameter. Using the full aperture of the ground telescope to transmit the beam increased the received signal strength by minimizing the beam divergence of the outgoing beam, thereby concentrating a much greater fraction of the laser pulse energy on the satellite. Adopting this approach in NASA's photon-counting SLR2000 system [6] increased measurement rates from under 10 Hz to 2 kHz and, due to significantly lower transmitted pulse energies and large transmitted beamwidths, greatly reduced eye safety hazards to aircraft. In this instance, using Equation (2), we can rewrite the original link equation, Equation (1), as [7,8]

$$\begin{aligned} n_s &= n_t(\eta_t\,\eta_r\eta_d)T_{atm}^2\left(\frac{4\pi A_p}{\lambda^2}\right)g_T\,\frac{\sigma A_p}{4\pi R^2}g_R \\ &= n_t(\eta_t\,\eta_r\eta_d)T_{atm}^2\left(\frac{\pi D_p^2}{\lambda^2}\right)g_T\,\frac{\pi^3\,\rho\,{D_{cc}}^4}{4\lambda^2}\,\frac{D_p^2}{4R^2}g_R \\ &= n_t(\eta_t\,\eta_r\eta_d)T_{atm}^2\left(\frac{\pi}{2}\right)^4\left(\frac{D_{cc}D_p}{\lambda R}\right)^4\rho g_T g_R \le 0.034 n_t T_{atm}^2\left(\frac{D_{cc}D_p}{\lambda R}\right)^4 \end{aligned} \tag{16}$$

where ρ is the reflectivity of the retro surfaces discussed in Section 2, n_t is the number of transmitted photons per laser pulse, $\eta_t \cong \eta_r \cong 0.66$ are the nominal optical throughput efficiencies of a telescope with aluminum- or silver-coated primary and secondary mirrors (plus a few additional low-loss optical elements) in the transmit and receive paths [20], η_d (<0.70) is the detector's counting efficiency, T_{atm} is the one-way transmission of the atmosphere, D_{cc} is the retro diameter, D_p is the diameter of the telescope's primary mirror, λ is the laser wavelength, R is the target range, and g_T ($\le$0.81) and g_R ($\le$1) are the reductions in the optimized transmitter and receiver gains due to the truncation of the outgoing quasi-

Gaussian beam by the primary mirror perimeter and/or the presence of a secondary mirror that blocks the central portion of the outgoing and incoming radiation [7,8].

Solving for n_t in Equation (16) and multiplying by the photon energy, hc/λ, the laser pulse energy required to achieve the desired number of signal photons, n_s, is

$$E_t = n_t \frac{hc}{\lambda} \geq \frac{30}{T_{atm}^2} n_s \frac{hc}{\lambda} \left(\frac{\lambda R}{D_{cc} D_p} \right)^4 \quad (17)$$

From Equation (17), the advantages of utilizing shorter laser wavelengths (λ) and the full primary diameter (D_p) of the ground-based telescope to transmit the laser beam is immediately apparent [6]. This is especially true for LLR, where the product $\lambda R = (532 \times 10^{-9}$ m)$(3.844 \times 10^8$ m) =204.5 m^2 at the widely used 532 nm green wavelength of the frequency-doubled Nd:YAG laser. If we assume a lunar retro diameter D_{cc} = 100 mm and the Apollo telescope primary mirror diameter of D_p = 3.5 m used in both transmit and receive modes, then $D_{cc}D_p$ = 0.35m^2. Ignoring atmospheric transmission losses, the minimum number of transmitted photons required to achieve a single photon return is 30 $(\lambda R/D_{cc}D_p)^4$ = 30(204.5/0.35)^4 =3.5 $\times$ 10^{12} photons, corresponding to a minimum laser pulse energy of 1.3 μJ at 532 nm. A one-meter telescope, on the other hand, would require a minimum of 195 μJ to realize a single photon return.

It should be noted that the use of a 100 mm-diameter cube, as proposed by several international LLR investigators, increases the signal from a single 38 mm Apollo cube by a factor of (100 mm/38 mm)^4 = 48, or roughly a factor of 6 lower than the 300-retro Apollo 15 array response. It would take a single 158 mm cube to roughly match the Apollo 15 array cross-section. This value is in excellent agreement with Table 1 in [15]. Based on their simulations, the latter authors also concluded that only the y-axis of the hollow retro's three retro axes would have to be corrected by between 0.65 and 0.8 arcsec offset for velocity aberration. Chinese researchers, on the other hand, describe the design, manufacture, and testing of a larger 170 mm hollow retroreflector [17] with all three axes deviating from 90°.

Millimeter-Accuracy LEO-to-MEO satellites use large-radius spherical satellites to better match the incoming plane wave, minimize pulse spreading, and allow for more reflectors within the active area to increase the cross-section. One can minimize satellite pulse broadening by reducing the range of accepted incidence angles through the use of hollow cubes or by recessing the cubes (hollow or solid) in tubes drilled into the satellite. It should also be noted that incidence angles < 17° do not leak light in solid TIR reflectors. Finally, one must select cube diameters and clocking angles that best match the "α annulus"while favoring the response at high zenith (low elevation) angles, which is key to efficient array design.

GNSS and GEO satellites typically have a nadir face pointed near the Earth's center due to their other operational functions, e.g., Earth observation, communications, navigation, etc. Therefore, flat panels perform reasonably well but still exhibit reduced cross-sections and several hundred picoseconds of temporal spread at lower satellite elevation angles. Flat circular (rather than square or rectangular) arrays would largely eliminate azimuthal range biases, but replacing current flat panels by a sphere segment of comparable cross-section would further improve range accuracy at all observation angles.

Lunar Laser Ranging (LLR) The single large cube concept put forward by various international teams of investigators clearly has the beneficial effects of (1) better defining the point of reference on the lunar surface and (2) reducing the target-induced, angular-dependent, temporal spread of the return pulse. However, achieving the same (or larger) target cross-sections than are currently available with the Apollo 15 array would require single-retro diameters in excess of 160 mm. Furthermore, as the size of the single retroreflector grows, the divergence of the reflected beam decreases, and careful attention must be paid to velocity aberration effects due to lunar orbital motion and Earth rotation. Furthermore, Earth's rotation effects decrease with the increasing latitude of the ground station and peak at the point of closest approach to the lunar target.

Finally, unlike Earth-orbiting satellites, where the target of interest is surrounded by a vacuum, lunar arrays are surrounded by a lunar surface, which can potentially introduce additional unwanted laser or solar photons to the overall return signal and thereby potentially degrade the range measurement accuracy. Even if one uses the entire 3.5 m aperture of the largest Apollo Observatorytelescope to achieve the least divergent laser beam, the central lobe of the transmitted beam will span a diameter of roughly $2\lambda R/D_p$ = 2 (532 nm) (384.4 × 10^6 m)/3.5 m = 117 m, corresponding to an angular FOV of 0.3 µrad. We can estimate the number of detected photons reflected by the lunar surface by applying the lidar equation (Equation (1) in [20]), which applies to a Lambertian-diffuse-reflecting surface that fills the receiver Field of View (FOV). Under the latter assumption, the number of laser photons received from the lunar surface is estimated at

$$\begin{aligned} n_{LS} &= nt(\eta_t\,\eta_r\eta_d)T_{atm}^2\left(\tfrac{4\pi A_p}{\lambda^2}\right)g_T\rho_{LS}\tfrac{cos\theta}{\pi R^2}A_p g_R \\ &= n_t(\eta_t\,\eta_r\eta_d)T_{atm}^2 g_T g_R\rho_{LS}cos\theta\left(\tfrac{\pi^2}{4}\right)\left(\tfrac{D_p^4}{\lambda^2R^2}\right) \end{aligned} \tag{18}$$

where ρ_{LS} = 0.12 is the nominal reflectivity of the lunar surface at visible and near-infrared wavelengths and θ is the nominal surface slope as viewed by the Earth station's line of sight. Dividing Equation (18) by Equation (16), we obtain an estimated ratio of lunar surface returns vs. retro returns, i.e.,

$$\frac{n_{LS}}{n_s} = \frac{\rho_{LS}}{\rho}\,cos\theta\left(\frac{4}{\pi^2}\right)\frac{\lambda^2R^2}{D_{cc}^4} \tag{19}$$

The latter equation indicates that the overall lunar surface return greatly exceeds that of the reflector since $(\lambda R)^2 >> {D_{cc}}^4$ because, even when one uses the full aperture of the ground telescope to minimize laser beam divergence, the diameter of the illuminated surface typically spans hundreds of meters. However, the retro produces a "hot spot" in the return, which can be isolated spatially via a pinhole in the receiver FOV or, better yet, a multipixel SPAD (Single-Photon Avalanche Diode) array, which can detect the "hot spot" during target acquisition and drive it to the central pixel of the array in order to maximize the retro signal strength while simultaneously assigning the vast majority of the surface photons to other pixels in the array. Locating the Earth-facing retro near the perimeter of the lunar disk would drive the $cos\theta$ term in Equation (19) close to zero. The Southern lunar pole region might be a good choice since it is believed to be a potential source of water for future manned missions. In order to further minimize the impact of lunar surface returns on range accuracy to the target retro, the pixel FOV should be chosen as small as is practically possible for rapid target acquisition. It may even be advantageous to elevate the retro a known distance above the lunar surface to more clearly separate the retro returns from local surface returns that fall within the common pixel FOV.

Finally, a recent article by the LLR staff in Grasse, France, provides an interesting history of their evolving technology over decades of operations and their experiences with near-infrared wavelengths [21]. It should also be mentioned in closing that the LLR station in Grasse successfully tracked the Lunar Reconnaissance Orbiter (LRO) satellite using a 4 × 3 retroreflector array mounted on the anti-nadir side of the spacecraft [22].

Laser ranging throughout the solar system using conventional single-ended ranging to passive reflectors is unrealistic due to the R^{-4} signal loss in the link equation. However, precise ranging (as well as time transfer and wideband communications) can be accomplished using two-way asynchronous laser transponders equipped with transmitters and receivers on both ends of the link [23,24]. In this instance, the signal strength at either terminal varies only as $1/R^2$ as opposed to $1/R^4$. Furthermore, since most of the link burden (laser power or telescope aperture) can be carried by the Earth station, the space terminal can be relatively modest in size (submeter), weight, and power consumption [25]. The feasibility of the interplanetary transponder approach has already been demonstrated

in experiments conducted at the 1.2 m telescope at NASA Goddard Space Flight Center with a satellite enroute to Mercury at a distance of 22 million km [24], which produced a range accuracy estimated at 20 cm [25]. Three months later, a second one-way experiment with the Mars Orbiter Laser Altimeter (MOLA) at a distance of 80 million km [26] resulted in roughly 500 laser pulses being detected by the Mars orbiter lidar receiver. In the latter case, the laser in orbit about Mars was sadly no longer operational when the interplanetary transponder experiment was conducted.

Funding: No funding was provided in support of this paper.

Institutional Review Board Statement: Not Applicable.

Informed Consent Statement: Not Applicable.

Data Availability Statement: Not applicable.

Conflicts of Interest: The author declares no conflict of interest.

References

1. Plotkin, H.H.; Johnson, T.S.; Spadin, P.; Moye, J. Reflection of Ruby Laser Radiation from Explorer 22. *Proc. IEEE* **1965**, *53*, 301–302. [CrossRef]
2. Alley, C.O.; Chang, R.; Curry, D.; Mullendore, J.; Poultney, S.; Rayner, J.D.; Silverberg, E.; Steggerda, C.; Plotkin, H.; Williams, W.; et al. Apollo 11 Laser Ranging Retro-Reflector: Initial Measurements from the McDonald Observatory. *Science* **1970**, *167*, 368–370. [CrossRef] [PubMed]
3. Degnan, J.J. Millimeter Accuracy Satellite Laser Ranging: A Review. *Contrib. Space Geod. Geodyn. Technol.* **1993**, *25*, 133–162.
4. Wilkinson, M.; Schreiber, U.; Procházka, I.; Moore, C.; Degnan, J.; Kirchner, G.; Zhongping, Z.; Dunn, P.; Shargorodskiy, V.; Sadovnikov, M.; et al. The next generation of satellite laser ranging systems. *J. Geodesy.* **2019**, *93*, 2227–2247. [CrossRef]
5. Pearlman, M.R.; Noll, C.E.; Pavlis, E.C.; Lemoine, F.G.; Combrink, L.; Degnan, J.J.; Kirchner, G.; Schreiber, U. The ILRS: Approaching 20 years and planning for the future. *Proc. SPIE* **1997**, *93*, 2161–2180. [CrossRef]
6. Degnan, J.J.; McGarry, J.F. SLR2000 Eyesafe and autonomous single photoelectron satellite laser ranging at kilohertz rates. *Proc. SPIE* **1997**, *93*, 2161–2180.
7. Klein, B.J.; Degnan, J.J. Optical Antenna Gain 1. Transmitting Antennas. *Appl. Opt.* **1974**, *13*, 2134–2141. [CrossRef]
8. Degnan, J.J.; Klein, B.J. Optical Antenna Gain 2. Receiving Antennas. *Appl. Opt.* **1974**, *13*, 2397–2401. [CrossRef]
9. McGarry, J.F.; Hoffman, E.D.; Degnan, J.J.; Cheek, J.W.; Clarke, C.B.; Diegel, I.F.; Donovan, H.L.; Horvath, J.E.; Marzouk, M.; Nelso, A.R.; et al. NASA's Satellite Laser Ranging Systems for the 21st Century. *J. Geodesy* **2018**, *93*, 2249–2282. [CrossRef]
10. Dickey, J.O.; Bender, P.L.; Faller, J.E.; Newhall, X.X.; Ricklefs, R.L.; Ries, J.G.; Shelus, P.J.; Veillet, C.; Whipple, A.L.; Wiant, J.R.; et al. Lunar Laser Ranging: A Continuing Legacy of the Apollo Program. *Science* **1994**, *265*, 482–490. [CrossRef]
11. Smullin, L.D.; Fioco, G. Optical Echoes from the Moon. *Nature* **1962**, *194*, 1267. [CrossRef]
12. Arnold, D.; (Harvard University, Boston, MA, USA). Personal Communication, 2013.
13. James, B.; Battat, R.; Murphy, T.W.; Adelberger, E.G.; Gillespie, B.A.; Boyle, C.D.; McMillan, R.J.; Michelson, E.I.; Nordtvedt, K.; Orin, A.E.; et al. The Apache Point Observatory Lunar Laser-ranging Operation (APOLLO): Two Years of Millimeter-Precision Measurements of the Earth-Moon Range. *Publ. Astron. Soc. Pac.* **2009**, *121*, 29–40.
14. Otsubo, T.; Kunimori, H.; Noda, H.; Hanada, H. Simulation of optical response of retroreflectors for future lunar laser ranging. *Adv. Space Res.* **2010**, *45*, 733–740. [CrossRef]
15. Otsubo, T.; Kunimori, H.; Noda, H.; Hanada, H.; Araki, H.; Katayama, M. Asymmetric Dihedral Angle Offsets for Large-Size Lunar Laser Ranging Reflectors. *Earth Planets Space* **2011**, *63*, 13–16. [CrossRef]
16. Currie, D.; Dell Agnello, S.; Delle Monache, G.O.; Behr, B.; Williams, J.G. Lunar Laser Ranging Reflector Array for the 21st Century. *Nucl. Phys. B* **2013**, 217–228.
17. He, Y.; Liu, Q.; He, J.; Li, M.; Duan, H.; Ye, H.; Luo, J. Development of a 170-mm hollow corner cube retroreflector for the future lunar laser ranging. *Chin. Phys. B* **2018**, *27*, 100701. [CrossRef]
18. Williams, J.G.; Porcelli, L.; Dell'Agnello, S.; Mauro, L.; Muccino, M.; Currie, D.G.; Wellnitz, D.; Wu, C.; Boggs, D.H.; Johnson, N.H. Lunar Laser Ranging Retroreflectors: Velocity Aberration and Diffraction Pattern. *Planet. Sci. J.* **2023**, *4*, 89. [CrossRef]
19. Garattinia, M.; Dell'Agnelloa, S.; Currie, D.; Delle Monachea, G.O.; Tibuzzia, M.; Patrizia, G.; Berardia, A.; Bonia, A.; Cantonea, C.; Itagliettaa, N.; et al. Moonlight: A New Lunar Laser Ranging Retroreflector Instrument. *Acta Polytech.* **2013**, *53*, 821. [CrossRef]
20. Degnan, J.J. Photon-counting multi-kilohertz microlaser altimeters for airborne and spaceborne topographic measurements. *J. Geodyn.* **2002**, *34*, 503–549. [CrossRef]
21. Chabe, J.; Corde, C.; Torre, J.M.; Bouquillon, S.; Borgin, A.; Aimar, M.; Albanese, D.; Chavineau, B.; Mariey, H.; Martinot-Lagarde, G.; et al. Recent Progress in Lunar Laser Ranging at Grasse Laser Ranging Station. *Earth Apace Sci.* **2019**, *7*, 3. [CrossRef]

22. Mazarico, E.; Sun, X.; Torre, J.M.; Courde, C.; Chabe, J.; Aimar, M.; Mariey, H.; Maurice, N.; Barker, M.K.; Mao, D.; et al. First two-way laser ranging to a lunar orbiter: Infrared observations from the Grasse station to LRO's retroreflector array. *Earth Planets Space* **2020**, *72*, 113. [CrossRef]
23. Degnan, J.J. Asynchronous Laser Transponders for Precise Interplanetary Ranging and Time Transfer. *J. Geodyn.* **2002**, *34*, 551–594. [CrossRef]
24. Degnan, J.J. Multipurpose Laser Instrument for Interplanetary Ranging, Time Transfer, and Wideband Communications. *Photonics* **2023**, *10*, 98. [CrossRef]
25. Smith, D.E.; Zuber, M.T.; Sun, X.; Neumann, G.A.; Cavanaugh, J.F.; McGarry, J.F.; Zagwodzki, T.W. Two Way Laser Link over Interplanetary Distance. *Science* **2006**, *311*, 53. [CrossRef]
26. Abshire, J.B.; Sun, X.; Neumann, G.; McGarry, J.F.; Zagwodzki, T.; Jester, P.; Riris, H.; Zuber, M.; Smith, D. Laser pulses from Earth detected at Mars. In Proceedings of the Conference on Lasers and Electro-Optics and Quantum Electronics and Laser Science Conference, Beach, CA, USA, 21–26 May 2006; Optica Publishing Group: Washington, DC, USA, 2006; pp. 1–2.